



Detached eddy simulations of rising Taylor bubbles

H. Shaban, S. Tavoularis*

Department of Mechanical Engineering, University of Ottawa, 161 Louis Pasteur, Ottawa, ON K1N 6N5, Canada

ARTICLE INFO

Article history:

Received 13 April 2018

Revised 12 June 2018

Accepted 15 June 2018

Available online 28 June 2018

Keywords:

Two-phase flow

Taylor bubble

Slug flow

DES

Coalescence

ABSTRACT

A numerical study of turbulent flow induced by Taylor bubbles rising in a stagnant liquid column is presented in this paper. Predictions of the void fraction, mean velocity and turbulent fluctuations are compared with available experimental results. In addition, we analysed the wall pressure and differential wall pressure fields as well as the temperature field produced by the interaction of a Taylor bubble with a heated tube wall. Implications for pressure measurements and thermal fluctuations in two-phase systems are discussed. A second simulation was performed to shed light on Taylor bubble coalescence, specifically highlighting the distinct mechanisms that operate in different parts of the wake region.

© 2018 Elsevier Ltd. All rights reserved.

1. Introduction

Slug flow is a regime of pipe flows of gas-liquid mixtures, in which the gas phase is contained mostly in so-called *Taylor bubbles*, which have characteristic bullet-like shapes and occupy most of the pipe cross-section. Adjacent Taylor bubbles are separated by liquid slugs, which may contain much smaller quasi-spherical or ellipsoidal gas bubbles. In vertical upwards flow, the net liquid flow is always upwards, but liquid may fall downwards in the annular space that surrounds each Taylor bubble. Slug flow occurs over wide ranges of gas and liquid flow rates and void fraction (Jones and Zuber, 1975), but may be absent from flows in pipes with diameters larger than a critical value that depends on the fluid properties (Taitel et al., 1980). Slug flows are encountered in many industrial devices, including oil and gas transport lines, nuclear reactor components and heat exchangers in power plants. In some applications, they may have detrimental effects, as for example pressure or thermal cycle damage caused by inherent flow pulsations. In other applications, the slug flow regime is desirable; an example is petroleum extraction using the gas-lift method, in which slugs transport large quantities of liquid (petroleum).

Because of their industrial importance, slug flows have been studied intensively both experimentally and numerically. In consequence of the fact that slug flows in oil and gas and nuclear power systems are generally turbulent, a number of experimental studies of slug flows have been performed under turbulent flow con-

ditions (Polonsky et al., 1999; Pinto et al., 2001; Van Hout et al., 2002). Several authors have reported wall pressure measurements in slug flows (e.g., Hewitt, 1978; Matsui, 1984; Sami and Lakis, 1986; Samways et al., 1997; Choutapalli and Vierow, 2010; Shaban and Tavoularis, 2014a; 2014b). Nevertheless, the collection of accurate in-flow measurements in many gas-liquid flows is difficult and, in some cases, impossible. An alternative approach is the use of numerical simulation, which can provide details not amenable to measurement. To this date, the vast majority of numerical simulations of rising Taylor bubbles have considered laminar flow conditions. For example, Bugg et al. (1998) solved a two-dimensional Volume-Of-Fluid (VOF) set of equations using a finite difference method to simulate a single bubble rising in a stagnant liquid column and examined the bubble shape for different combinations of Morton and Eötvös numbers. Anglart and Podowski (2002) simulated Taylor bubble coalescence in three-dimensional vertical laminar flow using the VOF method and their results agreed qualitatively with the observations of other researchers. Lu and Prosperetti (2009) applied a finite volume method, with the gas-liquid interface tracked using marker points, to study Taylor bubble properties under laminar conditions, whereas the thermal properties of Taylor bubble flow were numerically investigated by Asadolahi et al. (2011), who used the VOF method to model the laminar flow of a train of Taylor bubbles in a heated tube. Behafarid et al. (2015) and Taha and Cui (2006) conducted three-dimensional simulations of turbulent Taylor bubble flow in vertical and inclined channels, using the level-set method with DNS and the VOF method with the RNG k-epsilon turbulence model, respectively.

The interaction between adjacent Taylor bubbles is a phenomenon of great practical significance. Pressure drop, heat trans-

* Corresponding author.

E-mail addresses: hshab073@uottawa.ca (H. Shaban), stavros.tavoularis@uottawa.ca (S. Tavoularis).

fer, mixing, pipe vibrations and slug velocity depend strongly on bubble size and spacing, which in turn depend upon the bubble interaction mechanism. An important issue that arose in several earlier studies was the mechanism that accelerated the trailing bubble while it was outside the near wake of the leading bubble. For example, Dukler et al. (1985) developed a model to estimate the minimum stable liquid slug length, and connected this length to the recovery of the wall boundary layer in the wake of the leading bubble. They estimated it to be approximately $16D$ for air–water flow in a vertical tube with a diameter of 51 mm and cited experimental results by others, which reported minimum stable lengths between $20D$ and $24D$. On the other hand, several experimental investigators (Campos and Guedes de Carvalho, 1988; Ahmad et al., 1998; Van Hout et al., 2002), found the near wake to extend only to about $2D$ downstream of the leading bubble bottom. The bubble interaction mechanism in the far wake remains poorly understood.

The general objective of the present study is to contribute to the body of knowledge about turbulent gas–liquid slug flows. We present a set of numerical simulations of Taylor bubbles with turbulent wakes rising in stagnant water columns. The phases were modeled using the VOF method, while the turbulence was modeled using the Detached Eddy Simulation (DES) method. In the following sections, we will first summarize the numerical approach that was used and validate its accuracy vs. experimental results collected by Van Hout et al. (2002). We will then discuss the main features of the flow field and the turbulent wake, followed by an analysis and discussion of the influence of Taylor bubble flow on a passive temperature field and the wall temperature. Finally, we will examine the interaction between two consecutive Taylor bubbles and discuss the possible mechanisms that govern Taylor bubble acceleration and coalescence. We anticipate that this work will contribute to the understanding of turbulent slug flows, paving the way towards the simulation of many important industrial flows.

2. Computational procedures

2.1. Computational geometry and initial and boundary conditions

The present computational geometry approximated the experimental set-up of Van Hout et al. (2002), whose results we used for validation of our simulations. These authors collected Particle Image Velocimetry (PIV) measurements around Taylor bubbles rising in a tube with a diameter $D = 25$ mm, at an axial location that was $80D$ above the tube inlet. For economy of computational resources, our computational geometry comprised a circular tube with a length $L = 20D$ (Fig. 1).

For the single-bubble computations, the void fraction field was initialized with an air bubble comprising a cylindrical body and a hemispherical nose, whose tip was at a distance of $4D$ from the top of the computational domain. The total length of the initial bubble was set as $3.6D$, in an effort to match its volume with the estimated average bubble volume in the experiments of Van Hout et al. (2002). It is noted, however, that the latter estimate had some uncertainty, as experimental bubbles had non-uniform lengths and the authors did not specify exact dimensions. Then, the tube walls were set in downward motion with a fixed velocity U_b , which was adjusted by trial and error until the bubble became stationary in the vertical direction. Liquid was introduced at the top with the same downward velocity U_b and exited to a uniform pressure at the bottom. This technique of using a moving reference frame greatly reduced the computational demands of the simulations and has been previously applied for Taylor bubble simulations by Taha and Cui (2006) and Lu and Prosperetti (2009), among others. The no-slip boundary condition was applied at the moving walls, while an advective boundary condition was applied at the bottom outlet of the computational do-

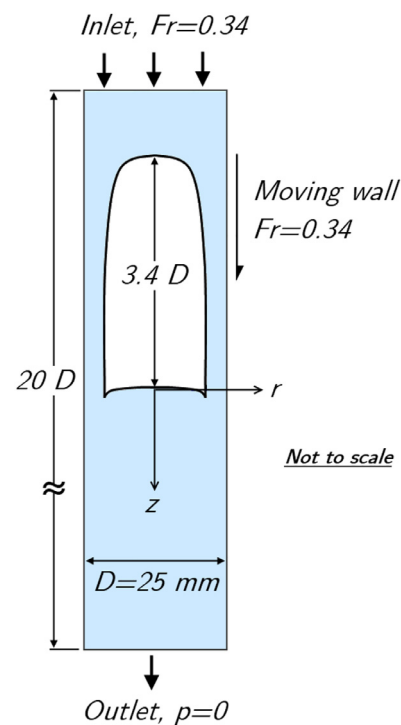


Fig. 1. Computational geometry and boundary conditions for a single Taylor bubble.

main. Additionally, a passive temperature field was also modelled with a constant heat flux applied at the walls. Surface tension was specified as 0.0728 N/m, which is the value for air–water mixtures at atmospheric pressure and 20°C . For consistency with the results presented by Van Hout et al. (2002), we set the origin of our coordinate system at the tail of the Taylor bubble as shown in Fig. 1.

2.2. Numerical model

All simulations were performed with the use of open-source Computational Fluid Dynamics (CFD) code OpenFOAM 2.3 (The OpenFOAM Foundation, 2014). OpenFOAM is a collection of C++ libraries, which can be used to tackle a variety of physical problems by solving sets of partial differential equations. In particular, we used InterFOAM, a two-phase incompressible flow solver in OpenFOAM, which solves the two-phase equations of flow on collocated grids using finite volume discretization. The VOF model implemented in InterFOAM solves a transport equation for the liquid volume fraction with certain modifications that counteract numerical diffusion and allow the modeling of a sharp interface. Unlike traditional VOF, the sharpening of the interface is not done using interpolation functions at the sub-grid level. Instead, the advection term in the volume fraction transport equation is modified, such that the interface sharpening is accomplished implicitly. InterFOAM has been used to simulate a variety of two-phase flow problems (e.g., Berberovic et al., 2009; Gopala et al., 2011; Trujillo et al., 2011). The phase distribution is handled using a modified VOF approach, first proposed by Ubbink (1997), which includes a compressive flux term that counteracts the smearing of the interface due to numerical diffusion. This numerical term allows the reconstruction of a sharp interface between fluid phases, making InterFOAM suitable for modelling gas–liquid two-phase flows. The theoretical foundations of the InterFOAM solver were recently presented by Deshpande et al. (2012). These authors also validated the InterFOAM solver using different kinematic tests and found that it could simulate accurately unsteady two-phase flows using moderately refined meshes.

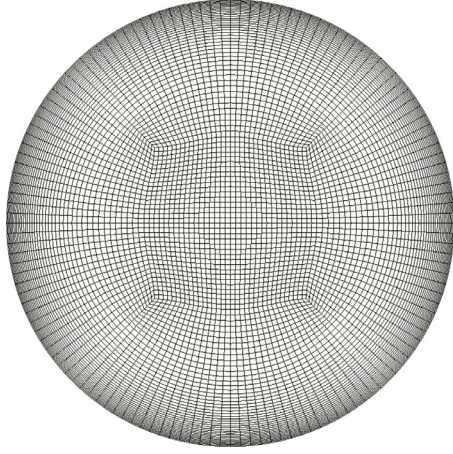


Fig. 2. Cross section of computational mesh.

The governing momentum equation is expressed as follows:

$$\frac{\partial}{\partial t}(\rho \mathbf{V}) + \nabla \cdot \rho \mathbf{V} \otimes \mathbf{V} = -\nabla P + \nabla \cdot [\mu (\nabla \mathbf{V} + \nabla \mathbf{V}^T)] + \rho \mathbf{g} + \mathbf{F}_{ST}, \quad (1)$$

with fluid properties calculated using the weighted (by volume fraction) mean of the properties of the two fluids.

In the OpenFOAM implementation of the Volume of Fluid method, the liquid volume fraction is treated as a continuous field, modelled as

$$\frac{\partial}{\partial t} \alpha + \nabla \cdot (\mathbf{V} \alpha) = 0 \quad (2)$$

and the surface tension force for interfacial cells is computed with the use of the continuum surface force (CSF) model proposed by Brackbill et al. (1992) as

$$\mathbf{F}_{ST} = \sigma \kappa \nabla \alpha \quad (3)$$

where κ denotes the local interface curvature and σ is the surface tension.

To simulate time dependent turbulent flows, we adopted the Spalart-Allmaras Improved Delayed Detached Eddy Simulation (IDDES) model (Shur et al., 2008), as implemented in OpenFOAM. This model was capable of resolving the vortical structures in the wakes of the Taylor bubbles and the time dependent interaction between bubbles. The IDDES model solves a set of mean and turbulence equations, with the Reynolds-Averaged Navier-Stokes (RANS) formulation used in proximity to solid walls and Large-Eddy Simulation (LES) used in the core of the flow away from walls. The IDDES model was developed to tackle issues related to the transition from RANS to LES in the boundary layer in traditional Detached Eddy Simulations (DES). It also allows the simulation to behave like wall-modelled LES, when the grid resolution close to the wall meets certain criteria.

The tube cross-section was first discretized into rectangular elements forming an O-grid (Fig. 2). These elements were extruded in the axial direction, resulting in a three-dimensional cylindrical domain, composed solely of hexahedral elements. As part of a mesh dependence analysis, we compared the calculated values of pressure and velocity produced with the use of three different meshes, comprising 2, 6 and 8 million elements, and found that the corresponding values varied by less than 10% for the two finer meshes. Only results obtained with the finest mesh (namely, 8,000,000 elements) are reported in the following.

All simulations were run for approximately five flow-through times, which ensured the statistical convergence of the main flow quantities. Then, results were collected during an additional interval of five flow-through times for statistical analysis. In all simulations, the Courant number was limited to a maximum value of

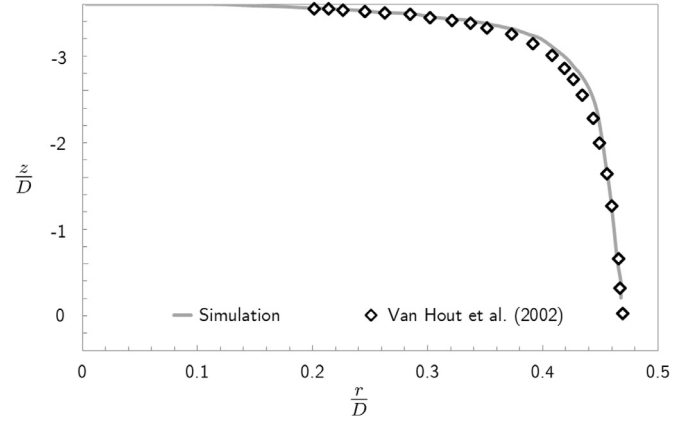


Fig. 3. Taylor bubble profile.

0.25, which corresponded to an average time step of 2×10^{-5} s. Each set of simulations required approximately six months of simulation time running on 192 processors provided by Calcul Qu  bec.

3. Flow field of a single Taylor bubble

3.1. Bubble shape

We first compare the computed shape and size of a single Taylor bubble rising in a stagnant liquid column with the experimental results. In both the experiments and the simulations, the bubbles were preceded and followed by liquid slugs and they were surrounded by a thin liquid film, which separated them from the tube wall. Van Hout et al. (2002) considered 100 bubbles and found that their average length was $3.6D \pm 8\%$, which is only about 5% larger than the bubble length $3.40D$ in the present simulations, so that the difference was within the experimental uncertainty. The average location of the bubble nose in fully developed flow remained approximately $4D$ downstream of the domain inlet. The bubble diameter in both the experiments and the simulations was found to increase gradually towards the tail of the bubble. The predicted shape of the Taylor bubble was nearly identical to the experimental one, as seen in Fig. 3. The bubble bottom was concave and oscillated in time, as expected for flows with relatively small viscous effects (Lu and Prosperetti, 2009).

3.2. The cross-sectional void fraction

In gas-liquid channel flows, the cross-sectional void fraction α represents the fraction of the channel area occupied by the gas phase. This quantity can be experimentally measured using tomography (e.g. X-ray tomographs) or by spatial averaging of point measurements of void fraction (e.g. wire-mesh sensors as used by Shaban and Tavoularis (2015, 2017a)). Fig. 4 shows the axial profile of α , which demonstrates that it rose very rapidly with increasing distance in the region between the nose of the bubble ($z/D = -3.4$) and a location near $z/D = -2.4$. It continued to rise, albeit at a much lower rate, until it reached a maximum value of 0.84 at the average location of the bubble bottom ($z/D = 0$), in conformity with the experimental observations of bubble shape shown in Fig. 3. Closely downstream of the bubble bottom, in the region $0 < z/D \lesssim 0.2$, where its value was affected significantly by the randomness of the bubble length and bottom shape, α had a rapid drop. Less predictably, it maintained a non-zero value in the entire computational domain, due to the presence of small spheroidal bubbles, which shed off the edges of the main Taylor bubble. Relatively close to the bubble bottom ($0.2 \lesssim z/D \lesssim 4$), α maintained

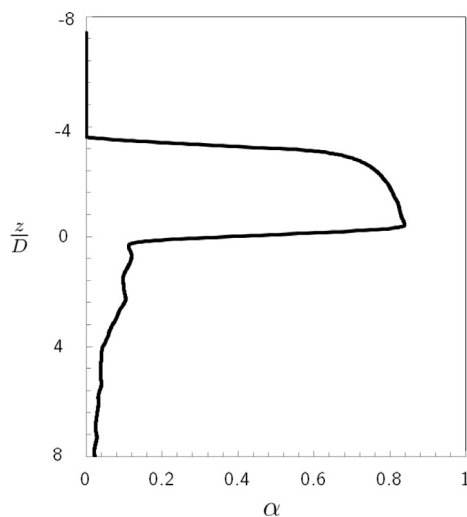


Fig. 4. Axial profile of the time-averaged cross-sectional void fraction.

significant levels ($0.02 \leq \alpha \leq 0.1$); in this region, some small bubbles became entrained in the recirculating toroidal vortex and re-coalesced with the main bubble. Beyond this region, α diminished further to a residual value of 0.01 at the downstream end of the computational domain. Once permanently detached from the Taylor bubble, some small bubbles rose with a speed that was lower than the liquid bulk velocity and they appeared to be convected outside the computational domain. The resulting continuous reduction of the length of the Taylor bubble within one flow-through time L/U_B was about 0.4%. As mentioned in Section 2.2, the time averages were collected over five flow-through times and the total reduction in bubble length during the averaging period was approximately 2%, which is far too small to have any measurable effect on the results reported in the following.

3.3. The mean velocity

As a Taylor bubble rises in a liquid column, liquid above it is displaced and flows downward through the annular film between the bubble and the tube wall. Because the thickness of this film is very small, the liquid in it moves with a relatively high velocity and exits the annular region as an annular jet, which generates a strong toroidal vortex in the immediate vicinity of the bubble bottom (Fig. 5). This is the location where the most intense mixing is anticipated to occur. As can be seen in Fig. 5 and Video 1 in the

supporting materials, the flow in the wake of the bubble is highly unsteady with smaller bubbles regularly shedding off the bubble bottom and re-coalescing with the main bubble when they get entrained in the toroidal vortex.

The bubble reaches its terminal velocity U_B when the drag force balances the buoyancy force. In the present simulations, we found $U_B = 0.170$ m/s, which is only 2% lower than the experimental value of 0.174 m/s reported by Van Hout et al. (2002). This corresponds to a Reynolds number $Re = U_B D / \nu \approx 4320$ (ν is the kinematic viscosity of water) and a Froude number $Fr = U_B / \sqrt{gD} \approx 0.34$. In the more general case of two-phase flows, Hayashi et al. (2011) proposed that the terminal velocity of the rising phase (expressed through the Froude number Fr) could be expressed as a function of the Reynolds number, the Etvs number and the viscosity ratio.

Fig. 6 shows the computed and experimental mean radial profiles of the axial \bar{V}_z and radial \bar{V}_r velocity components, normalised by the terminal velocity U_B , at several distances z from the bubble bottom plane. The computed values were shifted upwards by U_B , which referenced the velocity to the laboratory frame, thus allowing a direct comparison with the experimental values. It can be seen that the axial velocity was relatively large (up to about $6U_B$ at $z = 0.06D$) in the annular jet and the toroidal vortex region. Overall agreement between the two sets of results for the axial velocity was fairly good, with a maximum difference of less than 7% of the maximum velocity. The values of the radial velocity were much smaller than U_B . The agreement between the computed and measured radial velocities was fair qualitatively, although differences between corresponding values were significant, especially in the near wake ($z \leq 0.5D$). It is noted, however, that near-wake measurements in the water had relatively large uncertainty, caused by the interference of the gas phase, and that, in any case, the observed differences in \bar{V}_r were insignificant ($\leq 0.02 U_B$), by comparison to the local axial velocity.

The annular liquid jet was initially very thin ($\approx 0.05D$ at $z = 0.06D$), but it spread and decelerated quickly further downstream. This strong deceleration resulted in an adverse pressure gradient, which caused the jet to detach from the tube wall at around $z = 1.4D$. Beyond approximately $z = 2D$, the time-averaged axial velocities were not significantly different from zero, demarcating the lower boundary of the wake region. The computed bubble wake length was thus approximately $2D$, which is comparable to the Van Hout et al. (2002) value as well as other observations in the literature.

To gain insight into the near-wake flow field, we have plotted in Fig. 7 the axial profile of the time-averaged wall shear stress

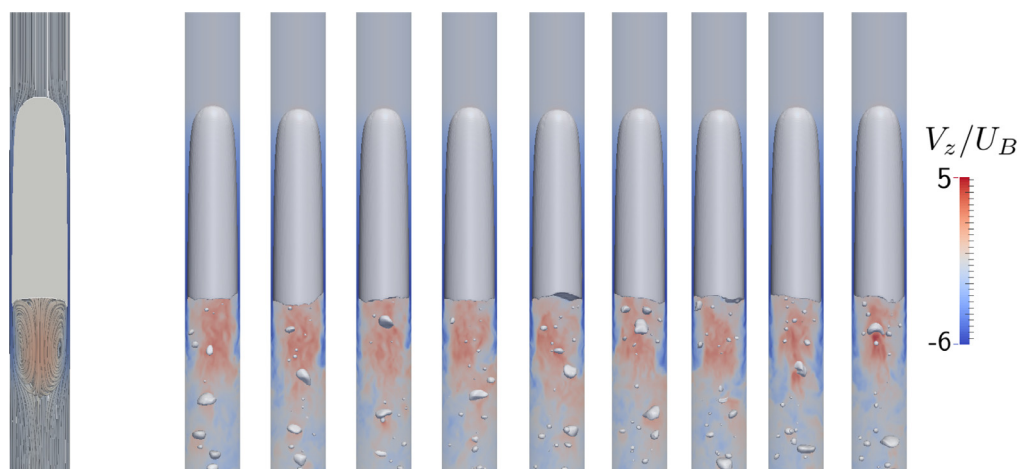


Fig. 5. Time-averaged streamlines (left) and nine representative instantaneous velocity contours (right).

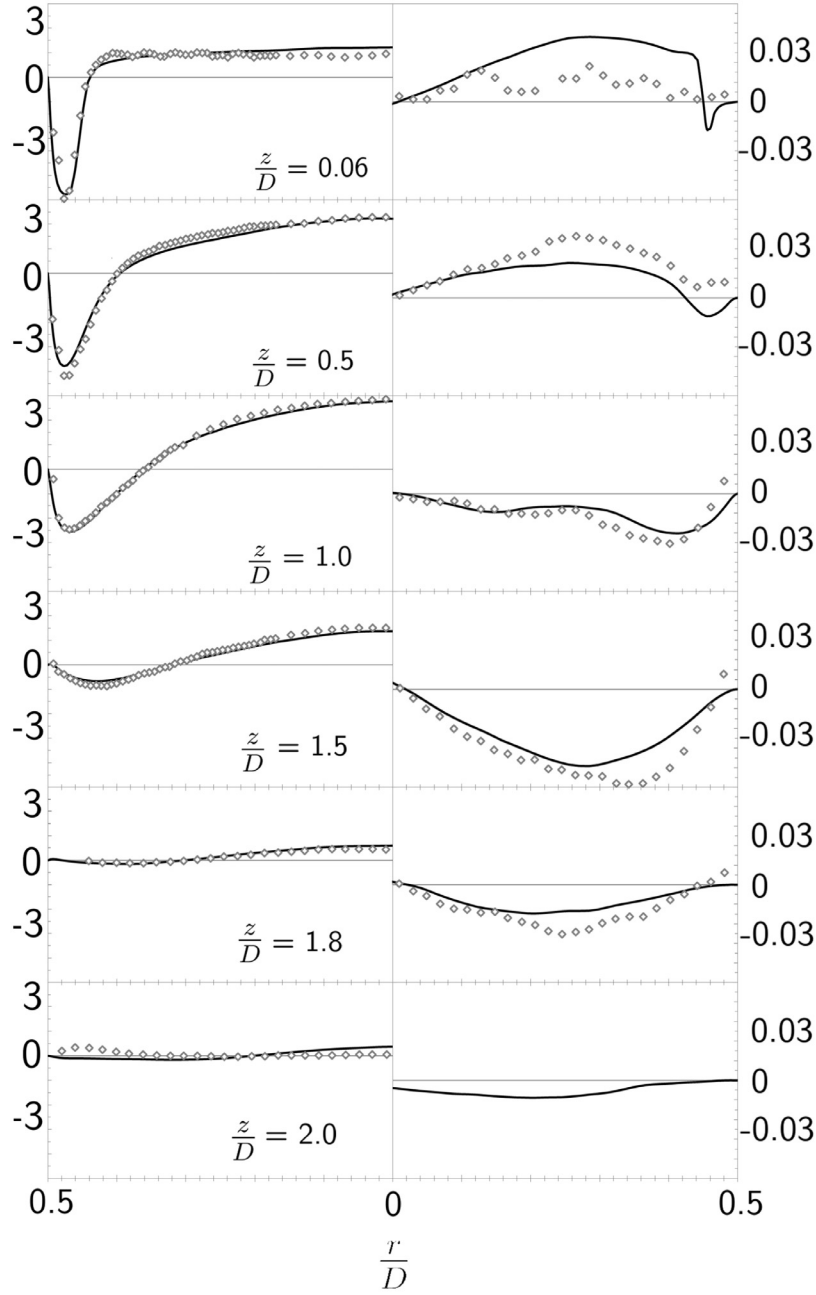


Fig. 6. Radial profiles of the normalised mean axial $\overline{V_z}/U_B$ (left column) and radial $\overline{V_r}/U_B$ (right column) velocity components behind the Taylor bubble in the present simulations (solid lines) and in the experiments by Van Hout et al. (2002) (symbols; no radial velocity data were reported for $z/D = 2.0$).

$\overline{\tau}_w$. A strong stress is observed along the part of the wall that surrounds the bubble. Starting from the level of the bubble nose, the wall shear stress rises, as the result of liquid acceleration along a progressively narrower annular region. Following a short distance of very rapid growth, which extends to approximately $1D$ downstream of the bubble nose, the rate of increase in $\overline{\tau}_w$ diminishes, as the thickness of the annular liquid region settles, until $\overline{\tau}_w$ reaches a local maximum near the bubble bottom. Further downstream, the liquid in the annular jet decelerates and the shear stress decreases until it vanishes at the separation point ($z \approx 1.4D$). Flow separation is followed by a very short recirculation region, reattachment and a region of weak upward flow, which extends to $z \approx 6D$ and is followed by essentially uniform flow.

3.4. The turbulence

Radial profiles of the normalised standard deviations of the axial and radial turbulent velocity fluctuations at different axial locations are shown in Fig. 8. The results shown correspond to the total Reynolds stresses, namely, the sum of the variances of the resolved velocity fluctuations and the sub-grid turbulent stresses obtained as outputs of the IDDES model. Beyond a distance of D from the bubble bottom, the computational and experimental results are in fair agreement, but, closer to the bubble, significant quantitative and qualitative differences between the two sets of profiles are visible. The simulations exhibit sharp peaks for both the axial and the radial fluctuation profiles in the shear layer between the annular jet and the recirculation zone, whereas a similar peak, although a much milder one, appears in the experimental profiles

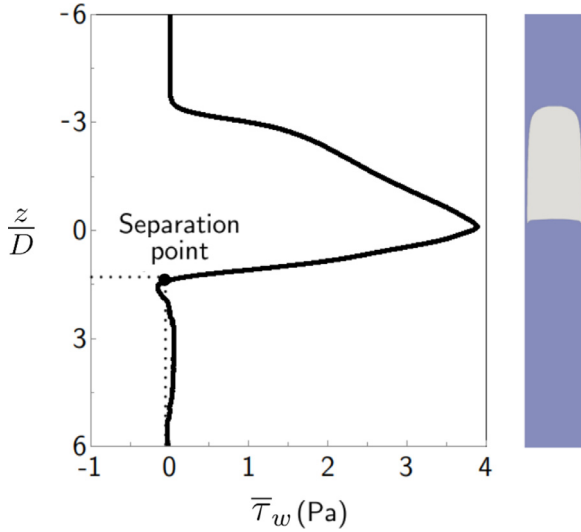


Fig. 7. Axial profile of the time-averaged wall shear stress.

of the axial fluctuations only. Moreover, the computational levels of fluctuations in the core of the very near wake are much lower than the measured levels. These differences may in part be caused by limitations of the numerical model employed, however, they may also be attributed in part to experimental inaccuracies (e.g., the relatively low spatial resolution of the PIV system, the contamination of turbulence fluctuations by strong differences among the characteristics of different bubbles and the oscillation of the bubble bottom in this region which may affect experimental accuracy), especially in the very near wake. The observed peaks become less prominent and move away from the wall as distance from the bubble is increased, as a consequence of the annular jet's expansion and the diminishing of the shear layer strength.

3.5. The wall pressure

In vertical air-water pipe flow, the hydrostatic pressure difference between two elevations at z_1 and z_2 would be

$$\Delta P_h = \int_{z_1}^{z_2} g[\rho_a \alpha + \rho(1 - \alpha)] dz, \quad (4)$$

where g is the gravitational acceleration, ρ_a is the density of air, α is the cross-sectional void fraction and ρ is the density of water. In still water, the pressure would increase downward at the liquid hydrostatic rate $dP_{h,l}/dz = \rho g$, whereas in air-water mixtures, in which $\rho_a < \rho$, the rate of hydrostatic pressure increase would be $dP_{h,lg}/dz \approx \rho g(1 - \alpha)$.

Fig. 9 shows the axial variation of the normalised wall pressure

$$P^* = \frac{P - P_{in}}{\rho g \Delta z_b}, \quad (5)$$

where P_{in} is the pressure at the inlet (set at zero) and $\Delta z_b \approx 6D$ is the length between $z = -4D$ and $z = 2D$ over which the rate of pressure increase deviated measurably from the liquid hydrostatic value, to be referred to as the domain of influence of the bubble. Both upstream and downstream of the domain of influence of the bubble, the wall pressure increased linearly at the liquid hydrostatic rate. By comparing extrapolated sections of the two linear segments in the P^* -plot, we found that the downward pressure increase across the domain of influence of the bubble was lower than the liquid hydrostatic pressure increase in the same section by an amount corresponding to a column of water equal to $2.81D$, which is significantly smaller than the length of the bubble ($3.40D$). The

pressure increase in the $3.40D$ -long pipe segment surrounding the bubble corresponded to that in a $0.21D$ -long liquid column. The pressure change across the bubble is largely due to the presence of the liquid film surrounding the bubble, which introduced some liquid hydrostatic pressure increase across the bubble body.

In addition to hydrostatic effects, pressure in multi-phase flows is subjected to several other influences, including viscous losses, surface tension effects and pressure fluctuations resulting from the breakup and coalescence of bubbles. Neglecting interfacial forces in air-water slug flows, one may estimate viscous pressure loss from the average wall shear stress as

$$\Delta P_v = \frac{4}{D} \int_{z_1}^{z_2} \tau_w dz. \quad (6)$$

The viscous pressure loss across the entire computational domain, estimated from Eq. (6), corresponded to that in a $0.18D$ -long liquid column and was therefore relatively small. 73.3% of the viscous pressure drop occurred in the film surrounding the bubble ($z < 0$), 27.2% of it occurred in the near wake up to the separation point ($0 \leq z \leq 1.4D$) and there was a small pressure recovery of 0.5% due to reverse flow in the far wake ($1.4D \leq z \leq 2D$).

The pressure variation downstream of the bubble was fairly complex. In the near wake ($0 \leq z \leq 0.7D$), the pressure increased quasi-linearly at a rate of approximately $0.7\rho g$. The difference between this and the liquid hydrostatic rate is attributed to viscous pressure loss associated with strong recirculation. Further downstream ($0.7D \leq z \leq 2D$), pressure recovery associated with flow deceleration overwhelmed viscous loss and the pressure increased rapidly, with its rate of increase reaching a maximum just upstream of the separation point ($z \approx 1.3D$), which appears as an inflection point in the pressure profile.

3.6. Differential wall pressure

The present analysis also allows us to examine the effect of bubble passage on the difference between the pressures at two wall locations separated by a relatively small axial distance. This pressure difference, measured by a differential pressure transducer connected to two taps, has been used in the past for gas-liquid flow regime identification (Matsui, 1984; Shaban and Tavoularis, 2014a) and void fraction measurements (e.g. Jia et al. (2015)). Differential pressure transducers are much more cost effective and much less intrusive than other void fraction measurement devices, including gamma-ray densitometers, X-ray tomographs and conductivity sensors.

A dimensionless differential pressure parameter was defined as

$$\Delta P^* = 1 - \frac{\Delta P}{\Delta P_{l,s}}, \quad (7)$$

where ΔP is the pressure difference between two wall locations separated axially by a distance D and $\Delta P_{l,s}$ is the pressure difference between the same locations, but with the tube containing still water. Matsui (1984) has postulated that such a parameter would be approximately equal to the void fraction in the volume of the tube between the elevations of the previous two wall locations, namely, approximately zero or one in a tube section filled, respectively, with liquid or gas. On the other hand, viscous losses in the liquid would tend to make ΔP^* negative, and in such cases this parameter would not be a correct indicator of the void fraction, which is bounded between 0 and 1.

The axial profile of ΔP^* is shown in Fig. 9. Because the pressure was calculated in a frame of reference that was moving with the same axial velocity as the bubble, this profile is analogous to the time series of ΔP^* that would be measured across two stationary taps, while the bubble passed the measurement locations. The computed profile is in qualitative agreement with the measured

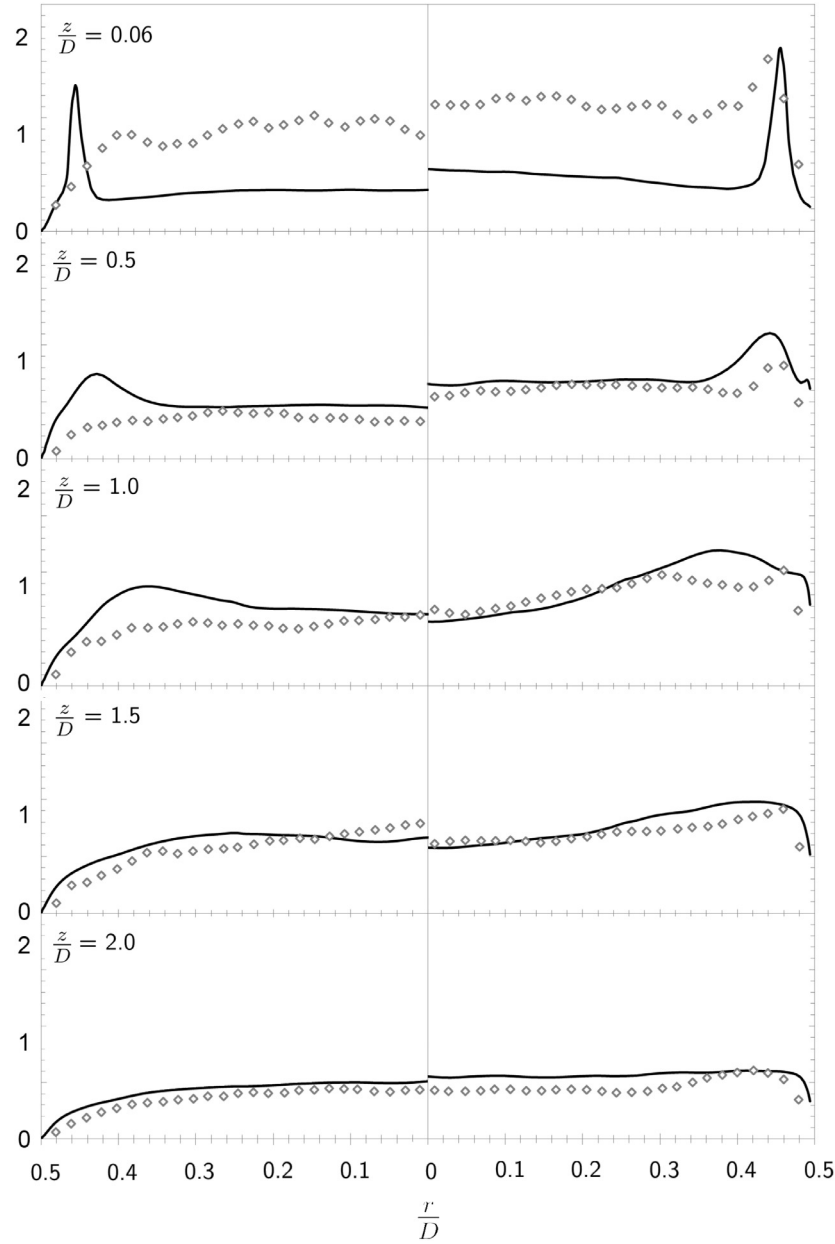


Fig. 8. Radial profiles of the standard deviations of the axial (left column) and radial (right column) velocity fluctuations behind the Taylor bubble in the present simulations (solid lines) and in the experiments by Van Hout et al. (2002) (symbols). All values have been normalised by U_B .

time series of ΔP^* in fully developed slug flow in a 32.5 mm diameter vertical tube, reproduced in Fig. 10 from an article by Shaban and Tavoularis (2014a,b). The computed profile of ΔP^* , and also in rough approximation the measured time series, have five distinct regions: a) $\Delta P^* \approx 0$ in the liquid slug upstream of the bubble; b) as the bubble nose is approached, ΔP^* rises rapidly; c) around the bubble, $\Delta P^* \approx 1$; d) in the wake, $\Delta P^* < 0$; and e) downstream of the wake, ΔP^* settles again at 0.

Estimates of average void fraction in slug flows that are based on measurements of ΔP^* are subject to two counter-acting types of error: a) a positive bias from the region around the bubble, where $\Delta P^* \approx 1$ whereas the cross-sectional void fraction never exceeded 0.93, and b) a negative bias from the wake region, where $\Delta P^* < 0$ whereas the cross-sectional void fraction is always non-negative. The total void fraction error for the volume contained between cross-sections at $z = -4D$ and $4D$ in the present configuration was found to be about -3%; this was computed as the percent

difference between the integral of ΔP^* between these two axial locations and the true average void fraction, which was about 0.37. This result indicates that the negative bias exceeded the positive one. Compensation for the negative bias by replacing negative values of ΔP^* by zeros resulted in a positive average void fraction error of 13%. In conclusion, one may assert that both the negative and the positive biases of ΔP^* are relatively small and so this parameter is a fairly accurate surrogate for void fraction in pipe flows, at least for the slug flow regime.

3.7. Wall temperature

Fig. 11 shows the axial variations of the non-dimensional wall temperature T^* and the Nusselt number Nu along the wall. These are defined as

$$T^* = k(T_{\text{wall}} - T_{\text{in}})/(q''D) \quad (8)$$

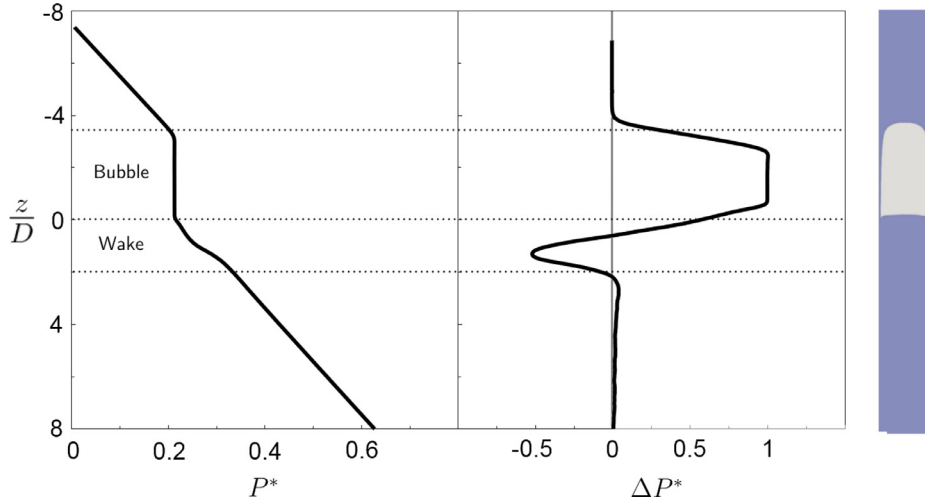


Fig. 9. Axial profiles of the time-averaged normalised wall pressure P^* (left) and the dimensionless differential pressure parameter ΔP^* (right).

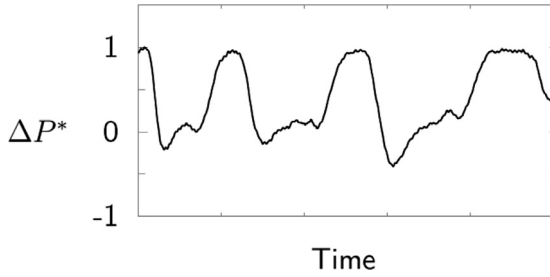


Fig. 10. Measured time history of normalised pressure ΔP^* in slug flow in a vertical tube (Shaban and Tavoularis, 2014a); the time axis has not been scaled, as this figure was intended to show typical pressure waveforms and not to serve for quantitative comparisons.

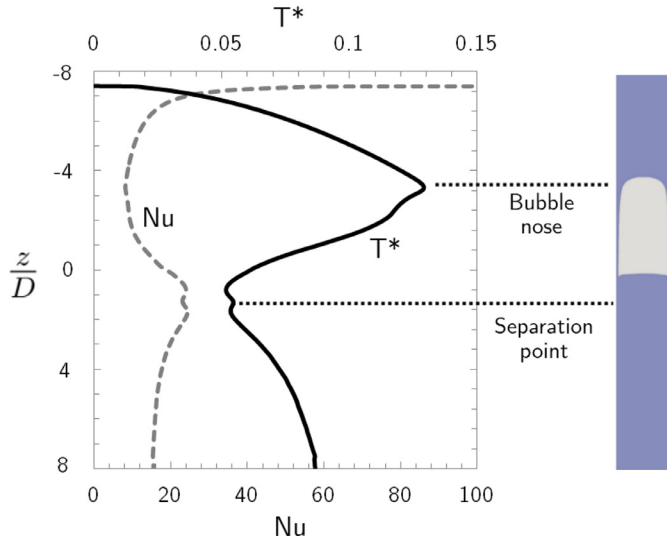


Fig. 11. Axial profile of wall temperature T^* and Nusselt number.

and

$$Nu = \frac{(q''D)}{k(T_{wall} - T_{bulk})}, \quad (9)$$

where k is the thermal conductivity of the water, T_{in} is the water temperature at the inlet of the domain, and T_{wall} , T_{bulk} and q'' are, respectively, the average wall temperature, fluid temperature and wall heat flux at each cross-section/axial location.

Near the top of the domain, T^* was small and Nu was very large, due to the absence of a thermal boundary layer. As this boundary layer developed, T^* increased and Nu dropped sharply. Near the Taylor bubble nose, the liquid accelerated as it entered the annular liquid film region and Nu increased gradually, while the wall temperature dropped accordingly. Near the Taylor bubble bottom, Nu increased again, following an increase in liquid velocity in the annular region, which reached values as large as $5U_B$. An inflection point in the axial profile of Nu is observed at the location where the liquid jet exited the annular region, beyond which the liquid decelerated. Nu peaked at an axial distance of approximately $1.4D$ from the Taylor bubble bottom. This location was found to correspond to the separation point of the liquid film, where the velocity gradient vanished (Shaban and Tavoularis, 2017b). This is also the location of minimum wall temperature. Downstream of this location, Nu gradually decreased and T^* gradually increased.

These observations have two main implications for the design and selection of materials for heat transfer systems that contain slug flows. First, it is clear that a slug flow would be accompanied by thermal cycling; in the case of a constant wall heat flux, wall temperature at a certain location would tend to decrease, while a Taylor bubble passed by, and increase again following passage of the bubble, while a liquid slug was present. The frequency and magnitude of these fluctuations depend on the length of the Taylor bubbles, the flow velocity and fluid properties. Secondly, the overall heat transfer in slug flows would be proportional to the length of the Taylor bubbles and wakes. Wake length is fairly insensitive to bubble length, whereas the bubble length is primarily influenced by the process of Taylor bubble coalescence, which will be discussed in the following section.

4. Coalescence of two Taylor bubbles

4.1. Methodology

A separate set of computations was performed in order to simulate the interactions between two consecutive Taylor bubbles. As a starting condition, we spliced together two sections of the computational domain, each containing the fully developed field of a single Taylor bubble. In particular, we retained the upstream section of this domain in the range $0 \leq z/D \leq 10$ and replaced the remainder by the upstream section of a duplicate single-bubble field. Thus, the total length of the computational domain was the same in both single- and double-bubble simulations and the nose of the trailing bubble was initially set at approximately $4.5D$ downstream

of the bottom of the leading bubble. The simulation was then started and run until the trailing bubble coalesced completely with the leading one. The evolution of the phase field will be described as a function of the dimensionless time $\tau = t/(L/U_B)$, where t is the physical time and the flow-through time that was used as time scale was $L/U_B = 2.94$ s.

4.2. Description of the coalescence process

To shed some light into the phenomena that occurred before and during Taylor bubble coalescence, we first identified the interfaces between the two Taylor bubbles and the surrounding water and then we computed the temporal variations of the location of the trailing bubble nose, the separation distance between the two bubbles and the trailing bubble velocity. We determined the location of gas-liquid interfaces by assuming that these interfaces coincided with void fraction iso-contours having a value $\alpha = 0.5$; these iso-contours were identified using the post-processing software Paraview 4.1 (www.paraview.org). To exclude small bubbles from the results, thus identifying only the two Taylor bubbles, we discarded any cavities that had a length along the tube axis that was smaller than $2D$. Next, we determined the instantaneous axial location $z_n(t)$ of the nose of the trailing bubble, which was assumed to be the most upstream location of the corresponding interface. This allowed us to compute the instantaneous separation distance Δz between the two bubbles as the distance between the time-averaged location of the leading bubble bottom along the tube axis and the instantaneous location of the nose of the trailing bubble. The transverse coordinates $r_n(t)$, $\theta_n(t)$ of the trailing bubble nose in a cylindrical coordinate system (r, θ, z) were recorded at all times. Because the trailing bubble deformed continuously, its motion cannot be described by a single parameter. To proceed, we approximated the vertical relative velocity of the trailing bubble by the temporal rate of change $d\Delta z/dt$ of the bubble separation distance. We also computed the radial and circumferential velocities of the bubble nose as dr_n/dt and $d\theta_n/dt$. Coalescence of the two bubbles was deemed to have occurred at the instant at which only a single iso-contour with $\alpha = 0.5$ that was longer than $2D$ could be identified.

Fig. 12a shows that the separation distance between the two Taylor bubbles decreased monotonically in time. The same figure also shows that it is possible to distinguish three stages in the relative motion of the trailing bubble, during each of which its relative velocity, plotted in Fig. 12 b was approximately constant, increasing markedly from one stage to the next. During the first stage ($0 \leq \tau \leq 0.55$, $4.5 \leq \Delta z/D \leq 4.0$), the bubble separation decreased very slowly ($d(\Delta z/D)/d\tau \approx 0.57$). A systematic investigation of the effect of initial separation distance on bubble coalescence was beyond the scope of the present study, and so it is not possible to affirm whether the end of this stage signifies a critical separation distance, the time it takes for disturbances in bubble eccentricity and/or nose shape to grow sufficiently, or a combination of these two effects. During the second stage ($0.55 \leq \tau \leq 0.80$, $4.0 \leq \Delta z/D \leq 2.2$), the relative velocity of the trailing bubble became significantly higher ($d(\Delta z/D)/d\tau \approx 6.8$). The third stage, which starts with the intrusion of the trailing bubble into the near wake of the leading bubble and ends with bubble coalescence ($2.2 \leq \Delta z/D \leq 0$), is characterised by an even higher rate of decrease of the separation distance ($d(\Delta z/D)/d\tau \approx 30.9$). It is noted that the computed relative velocity fluctuations were significant, especially during the third stage.

Snapshots of the shapes of the two Taylor bubbles at selected times during each of the three coalescence-process stages are shown in Fig. 13, whereas Video 2, included in the supplementary materials, is an animation of the entire process. During the first stage, the nose region of the trailing bubble underwent mild de-

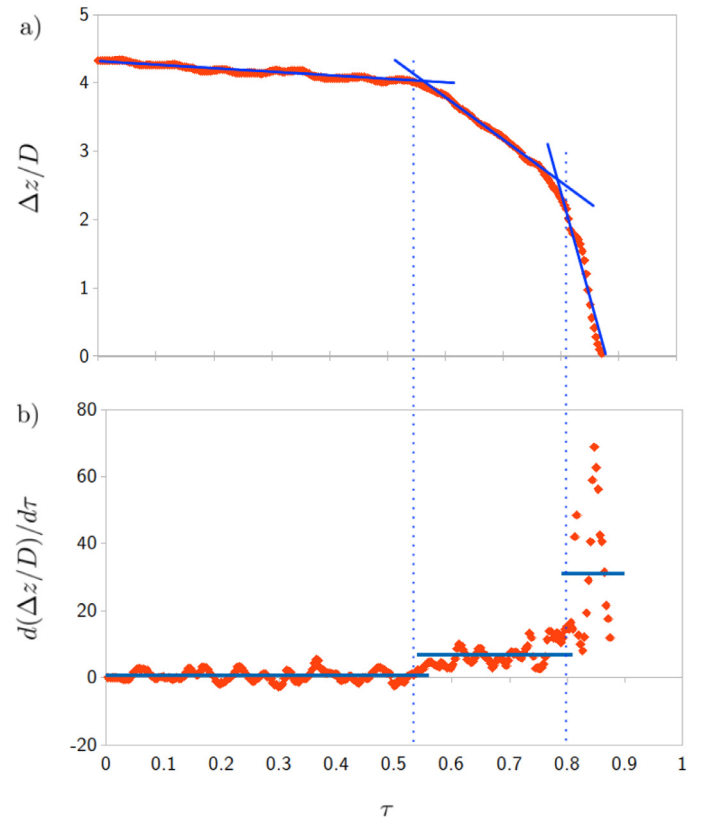


Fig. 12. Temporal variation of a) the bubble separation distance and b) the trailing bubble relative velocity; symbols mark calculated values; solid lines in (a) indicate least-squares linear fits to the data, whereas in (b) they denote the mean relative velocity (i.e., the mean slope of the bubble separation distance time series) in each stage of coalescence; dashed lines mark the boundaries between the three coalescence-process time intervals.

formations and swayed gently from side to side, while advancing slowly towards the leading bubble. During the second stage, the trailing bubble advanced towards the leading bubble at a markedly faster pace and its interface became unstable, first in the nose region and gradually over its entire length. The third stage started at the instant the trailing bubble entered the near wake of the leading bubble, which is indicated by contours of axial velocity shown in the images. As time advanced, the trailing bubble nose oscillated widely in all directions and a front portion of this bubble was detached from it and became engulfed into the leading bubble. This process was repeated rapidly until the entire trailing bubble coalesced with the leading bubble, thus forming a single, longer, Taylor bubble. The shape of the leading bubble does not seem to be affected significantly by the approach of the trailing bubble prior to coalescence.

The presently observed Taylor bubble coalescence process is in qualitative agreement with experimental observations by Zukoski (1966) and Shemer and Barnea (1987), among others. These authors have documented the radial displacement and deformation of the trailing bubble nose and correlated the trailing bubble rise velocity with the velocity profile in the near wake of the leading bubble. For reference, we (Fig. 6) and other experimental investigators (Campos and Guedes de Carvalho, 1988; Ahmad et al., 1998; Van Hout et al., 2002), found the near wake to extend to about $2D$ downstream of the leading bubble bottom. Thus, the presently observed start of the third stage of bubble coalescence coincided with the instant when the trailing bubble nose entered the leading bubble near wake. This stage includes the fissoning and engulfment of the trailing bubble, but the coales-

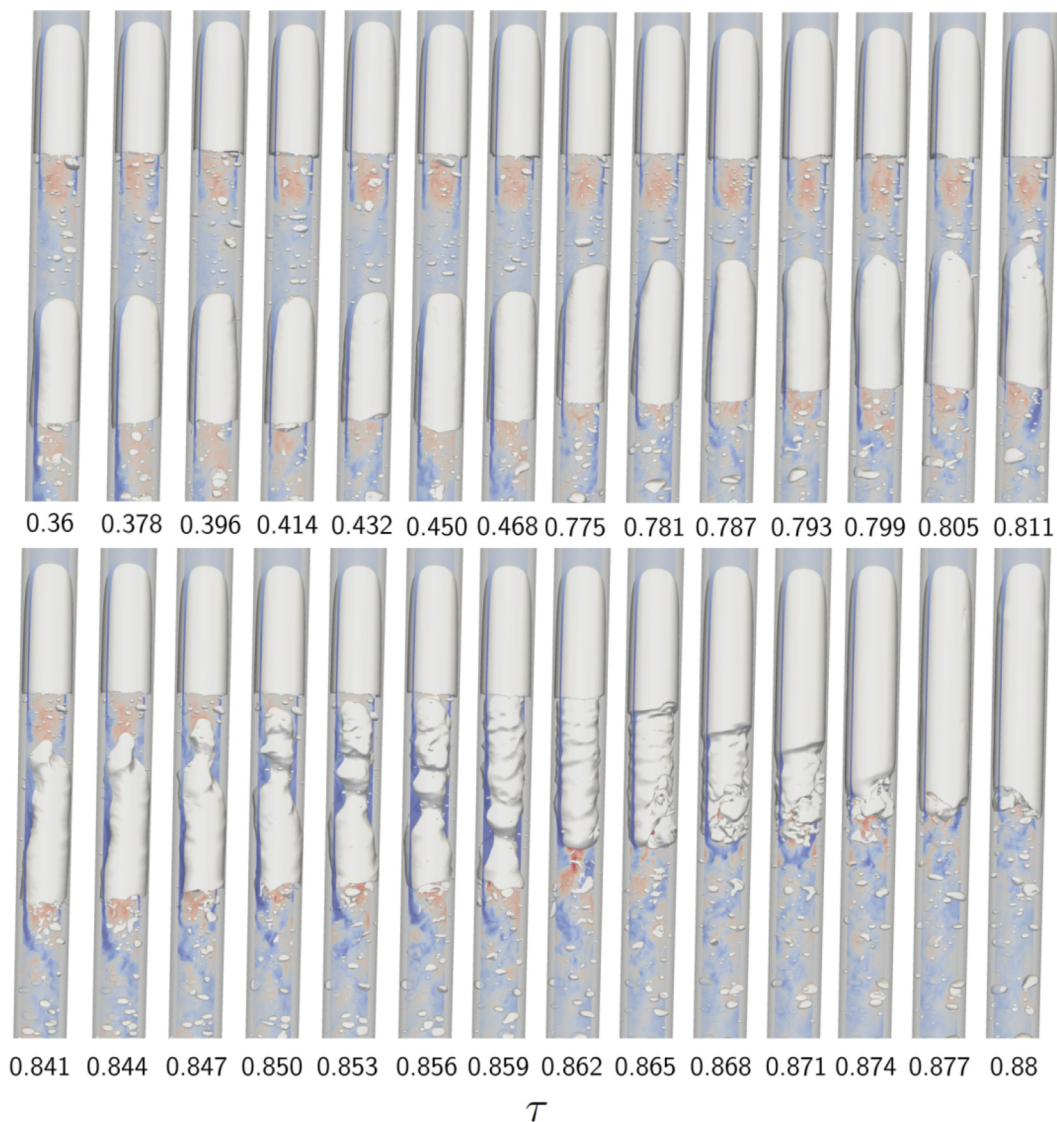


Fig. 13. Snapshots of Taylor bubble shapes during the three stages of coalescence; seven images on the left and right sides of the top row were taken during the first and second stages, respectively, whereas images in the bottom row were taken during the third stage; contours of axial velocity are also shown to indicate the extent of the near wakes of the bubbles.

cence mechanism was triggered as soon as the bubble was released, namely while the bubble nose was far outside the mentioned near wake. Although we did not determine the minimum initial separation distance between the two bubbles for the trailing bubble to approach the leading one, we can infer from the work of Dukler et al. (1985) that this distance is fairly large. These authors estimated theoretically the minimum stable liquid slug length, *i.e.*, the Taylor bubble separation distance that would ensure no bubble coalescence, as approximately $16D$ for air-water flow in a vertical tube with a diameter of 51 mm. They also cited experimental results by others, which reported minimum stable lengths between $20D$ and $24D$.

4.3. On the coalescence mechanism

In this section we will try to identify the physical causes of the phenomena that were observed during the coalescence process.

Trailing bubble deformation and radial displacement: In contrast to the leading bubble, which maintained a very stable shape, the trailing bubble underwent time-dependent deformation and radial displacement, especially in its nose region. The radial dis-

placement of the bubble nose had an average value of about $0.3R$, where R is the tube radius, but reached values exceeding $0.6R$. The time histories of the radial and azimuthal locations of the bubble nose did not indicate any systematic pattern. Bubble deformation and displacement are attributed to local, small-scale pressure fluctuations in the surrounding liquid, which necessarily originated in the shear layer around the leading bubble and its turbulent wake. Tudose and Kawaji (1999) postulated the presence of small-scale eddies far downstream of the leading bubble, whereas Van Hout et al. (2002) measured velocity fluctuations as far as $30D$ downstream of a Taylor bubble. Our results corroborate these observations: Fig. 14 shows that coherent structures downstream of a Taylor bubble, identified using the λ_2 criterion (Jeong and Hussain, 1995), maintained their strength at least $10D$ downstream of the bubble bottom; representative radial profiles of pressure plotted in the same figure show persisting localised regions with pressure fluctuations which were of the same order of magnitude as the pressure difference across the bubble interface, hence large enough to upset the balance of forces that governs the shape of the bubble interface. The fluctuating pressure force that acts on the interface of the trailing bubble tends to both deform the interface

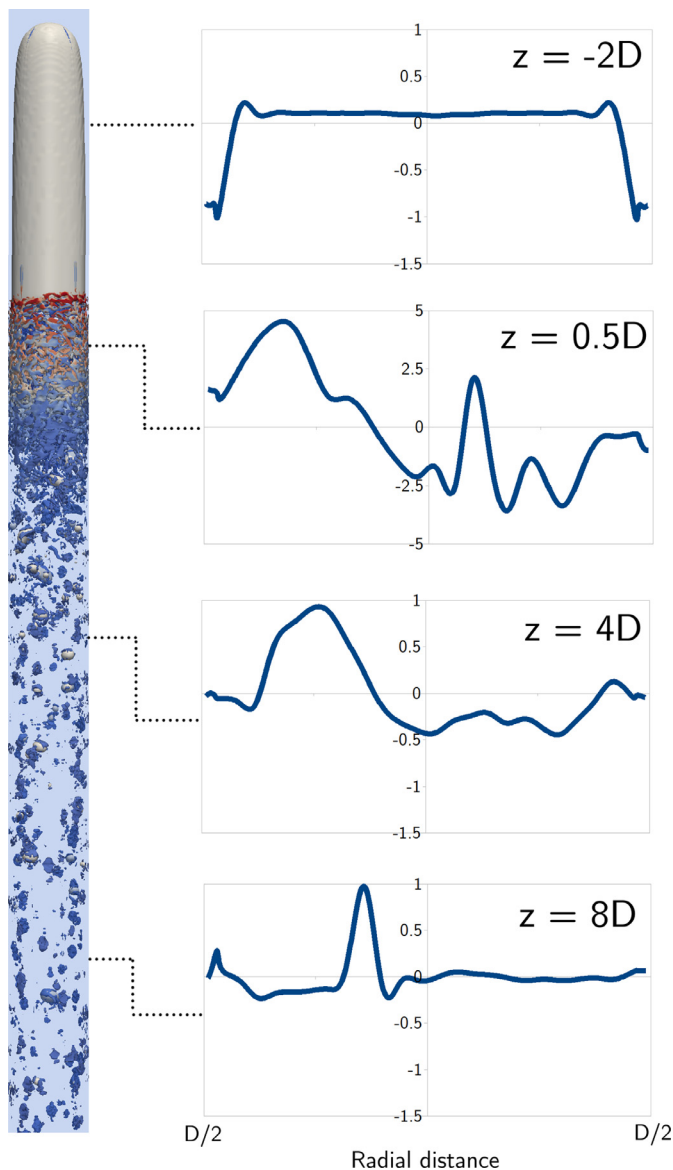


Fig. 14. Coherent structures identified using the λ_2 criterion (isocontours of $\lambda_2 = -1000$) downstream of Taylor bubble (left) and radial profiles of pressure at various axial distances (right). Pressure values have been centered at the average pressure for each cross-section and normalized by the pressure difference across the Taylor bubble interface.

and also shift it away from the tube axis, while the interfacial force opposes deformation.

Drag reduction and trailing bubble acceleration: Consequences of trailing bubble deformation and off-axis displacement are a decrease in the drag force on this bubble, an upward acceleration with respect to the leading bubble and a monotonic decrease of the separation distance between the two bubbles. This drag reduction is consistent with the well known fact that the friction factor in eccentric annular channels is lower than that in concentric ones with the same diameter ratio (Snyder and Goldstein, 1965) and the previous finding that the drag force on rigid bullet-shaped models of Taylor bubbles in tubes decreased with increasing eccentricity and increasing nose deformation (Tudose and Kawaji, 1999). The instantaneous drag force on the trailing bubble, computed as the axial component of the total pressure force on the bubble interface, had strong fluctuations, but, following an initial transitional interval ($0 \leq \tau \leq 0.2$), it maintained an average of roughly 90% of

the drag on the leading bubble. The drag was correlated negatively with the bubble nose relative velocity (the peak correlation coefficient was -0.27).

Trailing bubble breakup: During the second stage, the bubble became more elongated and its nose became narrower, which are indications that the nose region was moving faster than the rear of the bubble. As the relative velocity between sections of the bubble increased, the bubble tended to develop “necks”, which were intensified by surface tension, thus creating an unstable condition. This instability evolved rapidly during the third stage, when not only the nose region but the entire bubble appeared fragmented into smaller bubbles connected by narrow necks. It is noted that the bubble experienced much stronger pressure and shear stress fluctuations during the third stage than during the previous stages and as a result its drag had much larger fluctuations as well. The fragments of the bubble had roughly equal dimensions in the axial and radial directions, which implies that the most unstable wavelength of disturbances would be comparable to the tube diameter. This is much smaller than the estimated value of about $15D$ for the minimum unstable wavelength for annular flow instability (Brennen, 2005). A stability analysis of this problem is necessary to identify the sequence of events that lead to bubble deformation and breakup and the physical mechanisms that cause them.

5. Summary

In this paper, we have presented a numerical study of turbulent flow induced by Taylor bubbles rising in a stagnant liquid column. Predictions of the void fraction, mean velocity and turbulent fluctuations were in fair agreement with available experimental results. In addition, we analysed the wall pressure and differential wall pressure fields as well as the temperature field produced by the interaction of a Taylor bubble with a heated tube wall. It was observed that the wall pressure and temperature undergo large fluctuations during the passage of a bubble, a fact which has implications on the performance of two-phase thermal systems.

A second set of simulations was performed to shed light on the mechanisms governing Taylor bubble coalescence. It was assessed that coalescence was dominated by two distinct mechanisms. While the trailing bubble was in the far wake of the leading bubble, it was deformed and displaced radially through interactions with coherent structures; eccentricity of the trailing bubble resulted in drag reduction and upward acceleration with respect to the leading bubble. Once the trailing bubble entered the near wake of the leading bubble, the strong disturbances of the latter's recirculating vortex elongated the former's nose region, thus bringing the two bubbles in contact and enabling bubble coalescence by surface tension actions.

This study is the first to validate numerical simulations of Taylor bubbles with turbulent wakes against measurements of local flow velocity, turbulence intensity and bubble shape. Our simulations have demonstrated, for the first time, the existence of coherent structures far downstream of the Taylor bubble and illustrated the sequence of events that result in the coalescence of two consecutive Taylor bubbles with turbulent wakes. These results indicate that the use of the CFD solver OpenFOAM along with the Volume-Of-Fluid two-phase model and the IDDES turbulence model are promising for computing gas-liquid flows in industrial systems, at least for relatively low Reynolds numbers and relatively low turbulence intensities.

Acknowledgments

Financial support for this study was provided by the University Network of Excellence in Nuclear Engineering (UNENE) and the Natural Sciences and Engineering Research Council of Canada

(NSERC). The authors would like to thank the members of The OpenFOAM Foundation for making OpenFOAM freely available for research and Calcul Québec for providing the computational resources used for this study.

Supplementary material

Supplementary material associated with this article can be found, in the online version, at [10.1016/j.ijmultiphaseflow.2018.06.008](https://doi.org/10.1016/j.ijmultiphaseflow.2018.06.008)

References

- Ahmad, W., DeJesus, J., Kawaji, M., 1998. Falling film hydrodynamics in slug flow. *Chem. Eng. Sci.* 53, 123–130.
- Anglart, H., Podowski, M., 2002. Fluid mechanics of taylor bubbles and slug flows in vertical channels. *Nucl. Sci. Eng.* 140, 165–171.
- Asadolahi, A., Gupta, R., Fletcher, D., Haynes, B., 2011. CFD approaches for the simulation of hydrodynamics and heat transfer in taylor flow. *Chem. Eng. Sci.* 66, 5575–5584.
- Behafarid, F., Jansen, K., Podowski, M., 2015. A study on large bubble motion and liquid film in vertical pipes and inclined narrow channels. *Int. J. Multiphase Flow* 75, 288–299.
- Berberovic, E., van Hinsberg, N., Jakirlic, S., Roisman, I., Tropea, C., 2009. Drop impact onto a liquid layer of finite thickness: dynamics of the cavity evolution. *Phys. Rev. E* 79, 15. 036306
- Brackbill, J., Kothe, D., Zemach, C., 1992. A continuum method for modeling surface tension. *J. Comput. Phys.* 100, 335–354.
- Brennen, C., 2005. *Fundamentals of Multiphase Flow*. Cambridge University Press.
- Bugg, J., Mack, K., Rezakallah, K., 1998. A numerical model of taylor bubbles rising through stagnant liquids in vertical tubes. *Int. J. Multiphase Flow* 24, 271–281.
- Campos, J., Guedes de Carvalho, J., 1988. An experimental study of the wake of gas slugs rising in liquids. *J. Fluid Mech.* 196, 27–37.
- Choutapalli, I., Vierow, K., 2010. Wall pressure measurements of flooding in vertical countercurrent annular air–water flow. *Nucl. Eng. Des.* 240 (10), 3221–3230.
- Deshpande, S., Anumolu, L., Trujillo, M., 2012. Evaluating the performance of the two-phase flow solver interFoam. *Comput. Sci. Discovery* 5, 37. 014016
- Dukler, A., Maron, D., Brauner, N., 1985. A physical model for predicting minimum stable slug length. *Chem. Eng. Sci.* 40, 1379–1385.
- Gopala, V., Nijeholt, J., Bakker, P., Haverkate, B., 2011. Development and validation of a CFD model predicting the backfill process of a nuclear waste gallery. *Nucl. Eng. Des.* 241, 2508–2518.
- Hayashi, K., Kurimoto, R., Tomiyama, A., 2011. Terminal velocity of a taylor drop in a vertical pipe. *Int. J. Multiphase Flow* 37, 241–251.
- Hewitt, G., 1978. *Measurement of two Phase Flow Parameters*. Academic Press, NY.
- Jeong, J., Hussain, F., 1995. On the identification of a vortex. *J. Fluid Mech.* 285, 69–94.
- Jia, J., Babatunde, A., Wang, M., 2015. Void fraction measurement of gas–liquid two-phase flow from differential pressure. *Flow Meas. Instrum.* 41, 75–80.
- Jones, O., Zuber, N., 1975. The interrelation between void fraction fluctuations and flow patterns in two-phase flow. *Int. J. Multiphase Flow* 2, 273–306.
- Lu, X., Prosperetti, A., 2009. A numerical study of taylor bubbles. *Ind. Eng. Chem. Res.* 48, 242–252.
- Matsui, G., 1984. Identification of flow regimes in vertical gas–liquid two-phase flow using differential pressure fluctuations. *Int. J. Multiphase Flow* 10, 711–720.
- Pinto, A., Coelho Pinheiro, M., Campos, J., 2001. On the interaction of taylor bubbles rising in two-phase co-current slug flow in vertical columns: turbulent wakes. *Exper. Fluids* 31, 643–652.
- Polonsky, S., Barnea, D., Shemer, L., 1999. Averaged and time-dependent characteristics of the motion of an elongated bubble in a vertical pipe. *Int. J. Multiphase Flow* 25, 795–812.
- Sami, S., Lakis, A., 1986. Spectral analysis of wall pressure fluctuations in turbulent two phase flow. *J. Acoust. Soc. Am.* 80, 1392–1403.
- Samways, A., Bradbury, L., Bruun, H., 1997. Pressure measurements and convection velocity evaluations in two-phase flow. *Int. J. Multiphase Flow* 23 (6), 1007–1029. doi:10.1016/S0301-9322(97)00034-7.
- Shaban, H., Tavoularis, S., 2014a. Identification of flow regime in vertical upward air–water pipe flow using differential pressure signals and elastic maps. *Int. J. Multiphase Flow* 61, 62–72.
- Shaban, H., Tavoularis, S., 2014b. Measurement of gas and liquid flow rates in two-phase pipe flows by the application of machine learning techniques to differential pressure signals. *Int. J. Multiphase Flow* 67, 106–117.
- Shaban, H., Tavoularis, S., 2015. The wire-mesh sensor as a two-phase flow meter. *Meas. Sci. Technology* 26, 16. 015306
- Shaban, H., Tavoularis, S., 2017a. Performance evaluation of conductivity wire-mesh sensors in vertical channel flow. *Flow Meas. Instrum.* 54, 185–196.
- Shaban, H., Tavoularis, S., 2017b. Thermal characteristics of Taylor bubble flow. In: *Proceedings of the International Conference on Thermal Engineering and Applications, ICTEA 2017*, February 26–28, 2017, Muscat, Oman
- Shemer, L., Barnea, D., 1987. Visualization of the instantaneous velocity profiles in gas–liquid slug flow. *Phys. Chem. Hydr.* 8, 243–253.
- Shur, M., Spalart, P., Strelets, M., Travin, A., 2008. A hybrid RANS-LES approach with delayed DES and wall-modeled LES capabilities. *Int. J. Heat Fluid Flow* 29, 1638–1649.
- Snyder, T., Goldstein, G.A., 1965. An analysis of fully developed laminar flow in an eccentric annulus. *AIChE J.* 11 (3), 462–467.
- Taha, T., Cui, Z., 2006. CFD Modelling of slug flow in vertical tubes. *Chem. Eng. Sci.* 61, 676–687.
- Taitel, Y., Bornea, D., Dukler, A., 1980. Modelling flow pattern transitions for steady upward gas–liquid flow in vertical tubes. *AIChE J.* 26, 345–354.
- The OpenFOAM Foundation, 2014. *OpenFOAM 2.3*. www.openfoam.com.
- Trujillo, M., Alvarado, J., Gehring, E., Soriano, G., 2011. Numerical simulations and experimental characterization of heat transfer from a periodic impingement of droplets. *J. Heat Transf.* 133, 1–10.
- Tudose, E., Kawaji, M., 1999. Experimental investigation of taylor bubble acceleration mechanism in slug flow. *Chem. Eng. Sci.* 54, 5761–5775.
- Ubbink, O., 1997. *Numerical Prediction of Two Fluid Systems with Sharp Interfaces*. Imperial College, London, UK Doctoral dissertation.
- Van Hout, R., Gulitski, A., Barnea, D., Shemer, L., 2002. Experimental investigation of the velocity field induced by a taylor bubble rising in stagnant water. *Int. J. Multiphase Flow* 28, 579–596.
- Zukoski, E., 1966. Influence of viscosity, surface tension and inclination angle on motion of long bubbles in closed tubes. *J. Fluid Mech.* 25, 821–837.